energies

MDPI

Article

Study of Rotation Effect on Nanofluid Natural Convection and Heat Transfer by the Immersed Boundary-Lattice Boltzmann Method

Tianwang Lai, Jimin Xu, Xiangyang Liu * and Maogang He

Key Laboratory of Thermal Fluid Science and Engineering of MOE, School of Energy and Power Engineering, Xi'an Jiaotong University, Xi'an 710049, China

* Correspondence: lxyyang@mail.xjtu.edu.cn; Tel./Fax: +86-29-8266-3863

Abstract: Aiming to investigate the rotation effect on the natural convection and heat transfer of nanofluid, which has an important application in the control of heat transfer, the velocity field and temperature distribution inside the square cylinder with the rotating heat source in the center were numerically studied and presented in detail at different Hartman numbers and aspect ratios using the immersed boundary-lattice Boltzmann method. Then, the average Nusselt number on the surface of the heat source was calculated to compare the heat transfer rate in different cases. The results showed that the rotation would reduce the effect of gravity on the flow and suppress the heat transfer between the rotating heat source and nanofluid, while the external magnetic field would reduce the rotation effect on the flow and suppress or promote the heat transfer depending on the rotational speed and aspect ratio. Moreover, the smaller aspect ratio of the heat source to the square cylinder would enhance the heat transfer rate and make the retarding effect of magnetic field on rotation more apparent. In addition, the dimensionless rotational speed was proposed in this work, by which much computational time could be saved during the calculation of the immersed-boundary lattice Boltzmann method for the problem of rotation.

Keywords: IB-LBM; nanofluid; rotation effect; heat transfer

check for updates

Citation: Lai, T.; Xu, J.; Liu, X.; He, M. Study of Rotation Effect on Nanofluid Natural Convection and Heat Transfer by the Immersed Boundary-Lattice Boltzmann Method. *Energies* **2022**, *15*, 9019. https://doi.org/10.3390/en15239019

Academic Editors: Feng Zhang, Fuquan Deng and Daren Zheng

Received: 24 October 2022
Accepted: 24 November 2022
Published: 29 November 2022

Publisher's Note: MDPI stays neutral with regard to jurisdictional claims in published maps and institutional affiliations.

Copyright: © 2022 by the authors. Licensee MDPI, Basel, Switzerland. This article is an open access article distributed under the terms and conditions of the Creative Commons Attribution (CC BY) license (https://creativecommons.org/licenses/by/4.0/).

1. Introduction

In the past few decades, nanofluids have attracted the attention of many researchers due to their important industrial applications, including solar collectors, heat exchangers, high-performance boilers, chemical catalytic reactors, the polymer industry and metallurgy [1–5], which benefit from the fact that it is convenient to change the thermohydrodynamic characteristics of nanofluids and then control the heat transfer rate [6–9].

From this point, Hu et al. [10] numerically investigated the natural convection flows in an eccentric annulus filled by Cu–water nanofluid with a constant heat flux wall and found that the eccentricity and radial ratio have a significant effect on the average Nusselt number. Mahmoudi et al. [11] analyzed the effects of a magnetic field on nanofluid flow in a cavity with a linear boundary condition and noted that the heat transfer and fluid flow depend strongly upon the direction of the magnetic field. Sathiyamoorthy and Chamkha [12] studied the MHD (Magnetohydrodynamics) natural convection flow of liquid gallium in a square cavity and concluded that the magnetic field with an inclined angle would affect the flow and heat transfer rates in the cavity. Izadi et al. [13] reviewed the published studies about mixed convection of nanofluids in enclosures and concluded that the influences of the nanoparticles' volume concentration, Richardson and Reynolds numbers on heat transfer and thermal entropy generation.

At the same time, the study of fluid flowing over the rotational structure has received considerable attention because of its important role in controlling the mixed convection heat transfer in cavities [14] and numerous applications in engineering and industrial fields such

as thermal-power systems, aeronautical systems, medical equipment, gas turbine rotors, storage devices in computers, air cleaning machines, crystal growth processes and food-processing technology [15]. Jeyabalan et al. [16] numerically explored the magnetic dynamo action of thermal space-periodic convection in a horizontal plane layer of electrically conducting fluid rotating about the vertical axis. Chertovskih et al. [17] numerically simulated the magnetohydrodynamic convective attractors in a plane layer of conducting fluid with square periodicity cells and then explored the dependence of magnetic field generation on the rotation rate. Rashidi et al. [18] analyzed the entropy generation in steady MHD flow over a rotating disk in the presence of a uniform magnetic field, and the results showed that this model had an important application prospect in heat transfer enhancement inside thermal-power systems, novel nuclear space propulsion engines and renewable energy systems. Sheikholeslami et al. [19] investigated the MHD natural convection of nanofluid between a cold outer square cylinder and a heated inner circular cylinder and analyzed the different effects of Hartmann number, nanoparticle volume fraction, types of nanofluid, Rayleigh numbers and aspect ratios on the flow and heat transfer characteristics.

On the other hand, the new computational method, i.e., the immersed boundary-lattice Boltzmann method (IB-LBM), which combines and utilizes the most desirable features of the lattice Boltzmann and the immersed boundary methods, has constantly been developed to deal with the complex or moving solid-fluid boundary conditions [20]. Wu and Shu [21] proposed an implicit velocity correction-based IB-LBM that not only keeps the advantages of conventional IB-LBM, such as simplicity and smooth solutions, but also avoids the disadvantage of not accurately satisfying the non-slip boundary conditions. Hu et al. [22] adopted IB-LBM to treat the curved velocity and thermal boundary conditions in the simulation of natural convection inside a square enclosure with a heated cylinder covered by a porous layer. Similarly, Li et al. [23] applied IB-LBM to the curved velocity and thermal boundary conditions and then numerically studied the natural convection of Al_2O_3-H_2O nanofluids in a square enclosure with a stationary circular cylinder.

However, to our knowledge, the literature related to the effect of rotating the solid-fluid boundary on nanofluid natural convection and heat transfer is still scarce, which may be owed to the large amount of computational time for the fluid velocity corrections at all Lagrangian boundary points in every time step during the calculation of IB-LBM [24]. Therefore, the dimensionless rotational speed is introduced in the present work to save computational time, and then the velocity field and temperature distribution inside the square cylinder with the rotating heat source in the center were numerically studied and presented in detail at different Hartman numbers and aspect ratios, which may contribute to many applications such as hydrodynamic and convective nonlinear dynamos [16].

2. Problem Statement and Mathematical Model

2.1. Problem Statement

The schematic diagram of the problem studied in this work is shown in Figure 1. The heated circular cylinder with temperature T_h is rotating anticlockwise at a certain angular velocity ω in the center of the cold square cylinder with temperature T_c ($T_c < T_h$). Between the circular cylinder and the square cylinder is TiO_2-H_2O nanofluid with the TiO_2 volume fraction φ = 5%. In addition, the uniform magnetic field $\boldsymbol{B}$ and gravity field $\boldsymbol{g}$ are under consideration, where the orientation of the magnetic field forms an angle θ with the horizontal line, and the magnetic Reynolds number is assumed to be small so that the induced magnetic field and the Hall effect can be neglected [25–27]. Moreover, $\lambda = 2R / L$ denotes the aspect ratio, and the Hartman number Ha [28] denotes the intensity of the magnetic field ($Ha = 0$ means there is no magnetic field). The purpose of the present work is to investigate the effect of the angular velocity ω on the velocity field, temperature distribution and Nusselt number of nanofluid natural convection at different aspect ratios λ and magnetic field $\boldsymbol{B}$.

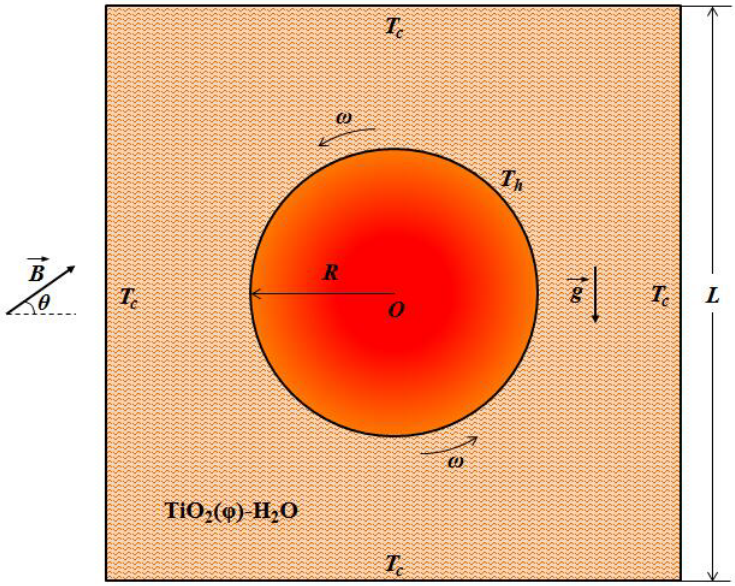

Figure 1. Schematic diagram of the problem in this work.

2.2. Thermophysical Properties of TiO_2-H_2O

The density ρ, specific heat capacity c_p, thermal conductivity k and dynamic viscosity μ of H_2O were calculated by REFPROP (version 9.1), and the density, specific heat capacity and thermal conductivity of TiO_2 were obtained from the literature [29], which are all shown in Table 1.

Table 1. Thermophysical properties of H_2O and TiO_2.

	ρ (kg·m^{-3})	c_p (J·kg^{-1}·K^{-1})	k (W·m^{-1}·K^{-1})	μ (Pa·s)
H_2O	995.7	4179.8	0.614	0.797×10^{-3}
TiO_2	4250.0	686.2	8.954	-

According to the literature [30], the thermophysical properties of TiO_2-H_2O can be calculated from the thermophysical properties of TiO_2 and H_2O as well as the volume fraction φ of TiO_2:

$$\rho_{nf} = \varphi \cdot \rho_s + (1 - \varphi) \cdot \rho_f \tag{1}$$

$$(\rho c_p)_{nf} = \varphi \cdot (\rho c_p)_s + (1 - \varphi) \cdot (\rho c_p)_f \tag{2}$$

$$k_{nf} = k_f\left(\frac{k_s + 2k_f - 2\varphi \cdot (k_f - k_s)}{k_s + 2k_f + \varphi \cdot (k_f - k_s)}\right) \tag{3}$$

$$\mu_{nf} = \frac{\mu_f}{(1 - \varphi)^{2.5}} \tag{4}$$

where the subscript of "*nf*", "*s*" and "*f*" denote the nanofluids, TiO_2 and H_2O, respectively.

2.3. Immersed Boundary-Lattice Boltzmann Method (IB-LBM)

In this work, the following lattice Boltzmann equation [31] was adopted:

$$f_i(\vec{x} + \vec{c_i} \cdot \Delta t, t + \Delta t) - f_i(\vec{x}, t) = -\frac{1}{\tau}(f_i(\vec{x}, t) - f_i^{(eq)}(\vec{x}, t)) + \Delta t \cdot F_i \tag{5}$$

where f_i is the density distribution function; $f_i^{(eq)}$ is the equilibrium distribution function; $\vec{x}$ is the position vector; $\vec{c_i}$ is the discrete lattice velocity in direction i; Δt is the lattice timestep; τ is the dimensionless lattice relaxation time for velocity; F_i is the force term determined by

the magnetic field, gravity and solid-fluid boundary together. The equilibrium distribution function $f_i^{(eq)}$ can be calculated by [32]:

$$f_i^{(eq)} = \omega_i \rho [1 + \frac{\vec{c_i} \cdot \vec{u}}{{c_s}^2} + \frac{\vec{u}\vec{u} : (\vec{c_i}\vec{c_i} - {c_s}^2 \boldsymbol{I})}{2{c_s}^4}] \tag{6}$$

where ω_i is the weighting factor; ρ is the lattice fluid density; $\vec{u}$ is the lattice fluid velocity; c_s is the lattice sound speed; $\boldsymbol{I}$ is the unit tensor. Moreover, the force term F_i can be calculated by [33]:

$$F_i = \omega_i \rho (1 - \frac{1}{2\tau})[\frac{\vec{c_i} \cdot \vec{F}}{{c_s}^2} + \frac{\vec{u}\vec{F} : (\vec{c_i}\vec{c_i} - {c_s}^2 \boldsymbol{I})}{{c_s}^4}] \tag{7}$$

where $\vec{F}$ is the net force of Lorentz force $\vec{F_L}$ caused by magnetic field, gravity $\vec{F_G}$ and force correction $\vec{F_C}$ caused by the solid-fluid boundary:

$$\vec{F} = \vec{F_L} + \vec{F_G} + \vec{F_C} \tag{8}$$

Lorentz force $\vec{F_L}(\vec{F_L} = F_{Lx} \cdot \vec{i} + F_{Ly} \cdot \vec{j})$ can be calculated by [34]:

$$\begin{cases} F_{Lx} = 3\omega_i \rho A(u_y \sin\theta \cos\theta - u_x \sin^2\theta) \\ F_{Ly} = 3\omega_i \rho A(u_x \sin\theta \cos\theta - u_y \cos^2\theta) \end{cases} \tag{9}$$

where A is corresponded to $Ha^2\nu$ / (ρL^2) and ν is the kinetic viscosity of fluid. The force correction $\vec{F_C}$ can be calculated by [21]:

$$\vec{F_C} = \frac{2\rho\delta\vec{u}}{\delta t} \tag{10}$$

where $\delta\vec{u}$ is the fluid velocity correction, which can be obtained from the boundary velocity correction $\delta\vec{u_B}$. The formula for $\delta\vec{u_B}$ is [35]:

$$\boldsymbol{AX} = \boldsymbol{B} \tag{11}$$

where

$$\boldsymbol{X} = \left\{\delta\vec{u_B^1}, \delta\vec{u_B^2}, \cdots, \delta\vec{u_B^m}\right\}^T \tag{12}$$

$$\boldsymbol{A} = \begin{pmatrix} \delta_{11} & \delta_{12} & \cdots & \delta_{1n} \\ \delta_{21} & \delta_{22} & \cdots & \delta_{2n} \\ \vdots & \vdots & \ddots & \vdots \\ \delta_{m1} & \delta_{m2} & \cdots & \delta_{mn} \end{pmatrix} \begin{pmatrix} \delta_{11}^B & \delta_{12}^B & \cdots & \delta_{1m}^B \\ \delta_{21}^B & \delta_{22}^B & \cdots & \delta_{2m}^B \\ \vdots & \vdots & \ddots & \vdots \\ \delta_{n1}^B & \delta_{n2}^B & \cdots & \delta_{nm}^B \end{pmatrix} \tag{13}$$

$$\boldsymbol{B} = \begin{pmatrix} \vec{U_B^1} \\ \vec{U_B^2} \\ \vdots \\ \vec{U_B^m} \end{pmatrix} - \begin{pmatrix} \delta_{11} & \delta_{12} & \cdots & \delta_{1n} \\ \delta_{21} & \delta_{22} & \cdots & \delta_{2n} \\ \vdots & \vdots & \ddots & \vdots \\ \delta_{m1} & \delta_{m2} & \cdots & \delta_{mn} \end{pmatrix} \begin{pmatrix} \vec{u_1^*} \\ \vec{u_2^*} \\ \vdots \\ \vec{u_n^*} \end{pmatrix} \tag{14}$$

Here, m denotes the number of Lagrangian boundary points and n denotes the number of surrounding Eulerian points; $\delta\vec{u_B^l}(l = 1, 2, \cdots, m)$ is the unknown velocity correction

vector at the Lagrangian boundary points; δ_{ij} is equal to $D_{ij}(\vec{x_{ij}} - \vec{x_B^l})\,\Delta x\Delta y$ and δ_{ij}^B is equal to $D_{ij}(\vec{x_{ij}} - \vec{x_B^l})\,\Delta s_l$ with the delta function $D_{ij}(\vec{x_{ij}} - \vec{x_B^l})$ expressed as:

$$D_{ij}(\vec{x_{ij}} - \vec{x_B^l}) = \delta(x_{ij} - x_B^l)\delta(y_{ij} - y_B^l) \tag{15}$$

$$\delta(r) = \begin{cases} \frac{1}{4}\left[1 + \cos\left(\frac{\pi|r|}{2}\right)\right], & |r| \le 2 \\ 0, & |r| > 2 \end{cases} \tag{16}$$

In addition, Δx and Δy both denote the lattice spacing; Δs_l denotes the arc length of the boundary element; $\vec{U_B^l}(l = 1, 2, \cdots, m)$ is the given velocity at Lagrangian boundary points; $\vec{u^*}$ is the intermediate fluid velocity, which can be calculated by:

$$\vec{u^*} = \frac{1}{\rho}\sum_i \vec{c_i} f_i \tag{17}$$

After the boundary velocity correction $\delta\vec{u_B^l}$ is obtained from Equations (11)–(17), the fluid velocity correction $\delta\vec{u}$ needed in Equation (10) can be calculated by:

$$\delta\vec{u} = \sum_{l=1}^{m} \delta\vec{u_B^l} D_{ij}(\vec{x_{ij}} - \vec{x_B^l})\Delta s_l \tag{18}$$

In the present work, D2Q9 model was used and then the discrete lattice velocity $\vec{c_i}$ in Equation (5) can be expressed as follows [36,37]:

$$\vec{c_i} = \begin{cases} (0,0) & k = 0 \\ c(\cos[(k-1)\pi/2], \sin[(k-1)\pi/2]) & k = 1,2,3,4 \\ \sqrt{2}c(\cos[(2k-1)\pi/4], \sin[(2k-1)\pi/4]) & k = 5,6,7,8 \end{cases} \tag{19}$$

where the streaming speed is defined as $c = \Delta x/\Delta t$. Moreover, the weighting factor ω_i can be expressed as [38]:

$$\omega_i = \begin{cases} 4/9 & i = 0 \\ 1/9 & i = 1,2,3,4 \\ 1/36 & i = 5,6,7,8 \end{cases} \tag{20}$$

Furthermore, $c_s = c/\sqrt{3}$ is the lattice sound speed in D2Q9 model, and the correctional bounce-back scheme was adopted in the boundary conditions, with the unknown distribution function in the boundary determined by:

$$\begin{cases} f^L{}_{1,5,8} = f^L{}_{3,7,6} \\ f^R{}_{3,6,7} = f^R{}_{1,8,5} \\ f^T{}_{4,7,8} = f^T{}_{2,5,6} \\ f^B{}_{2,5,6} = f^B{}_{4,7,8} \end{cases} \tag{21}$$

where the superscript "*L*", "*R*", "*T*" and "*B*", respectively, denote the left, right, top and bottom wall.

Finally, the fluid density ρ and velocity $\vec{u}$ can be calculated by [39]:

$$\rho = \sum_{i=0}^{8} f_i \tag{22}$$

$$\vec{u} = \vec{u^*} + \delta\vec{u} \tag{23}$$

The IB-LBM for energy equation is similar and introduced in detail in the literature [35], which is not described here. It is worth mentioning that the average Nusselt number on the solid-fluid boundary Nu is calculated by:

$$Nu = \frac{L}{\alpha \Delta t (T_h - T_c) L_s} \sum_{l=1}^{m} \delta T_B^l \Delta s_l \tag{24}$$

where α is the thermal diffusivity of fluid; L_s is the total length of boundary; δT_B^l (l = 1, 2, ⋯, m) is the temperature correction at the Lagrangian boundary points.

2.4. Minimum Angular Velocity and Dimensionless Rotational Speed

As shown in Figure 2, assuming that the boundary Lagrangian points (P_{i-1}, P_i, P_{i+1}, ⋯) are distributed at equal spacing at time t_0, the minimum angular velocity is defined as the minimum angular velocity, which makes P_i overlap with P_{i+1} at time $t_0 + \Delta t$. According to the definition, the minimum angular velocity $\omega_{\min}$ can be calculated by:

$$\omega_{\min} = \frac{2\pi}{m\Delta t} = \frac{2\pi\nu}{mL^2} \cdot \frac{L'^2}{\nu' \cdot \Delta t'} \tag{25}$$

where m is the number of Lagrangian boundary points and ν is the kinematic viscosity of fluid; the superscript means the physical quantities are expressed in physical units instead of lattice units. Since the elements of matrix $\boldsymbol{A}$ in Equation (13) are only related to the Lagrangian boundary points and their neighboring Eulerian points, the advantage of $\omega_{\min}$ is that a lot of computational time could be saved if the angular velocity of the rotating circular cylinder shown in Figure 1 was set to the integral multiple of $\omega_{\min}$ because the overall distribution of Lagrangian boundary points remains unchanged in this case and matrix $\boldsymbol{A}$ could be calculated before time iteration rather than during every time step.

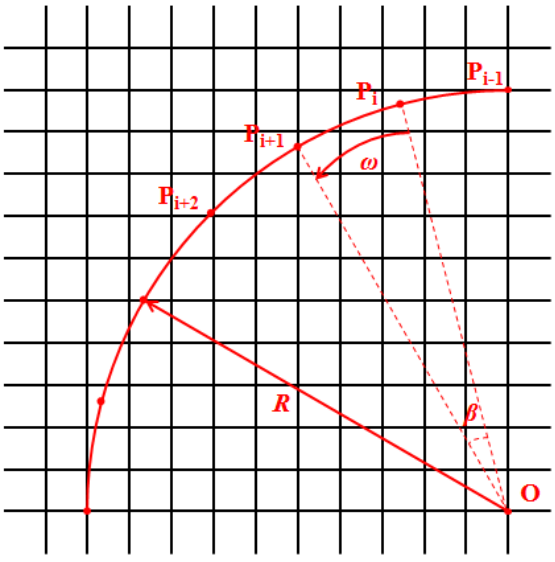

Figure 2. Schematic diagram of minimum angular velocity.

However, it is inconvenient for $\omega_{\min}$ to apply in the practical computation due to the variables of L', ν' and $\Delta t'$ in different initial and boundary conditions. Therefore, the dimensionless rotational speed N is proposed and can be calculated by:

$$N = \frac{\omega}{m\omega_{\min}} \cdot \frac{L'^2}{\nu' \cdot \Delta t'} = \frac{\omega L^2}{2\pi\nu} \tag{26}$$

where $m\omega_{\min}$ can be interpreted as the minimum angular velocity, which makes P_i rotate for one cycle and overlap with itself at time $t_0 + \Delta t$, while $L'^2/(\nu' \cdot \Delta t')$ can be regarded as

the positive and dimensionless factor. Apparently, the dimensionless rotational speed N not only keeps the advantage of saving much computational time during the calculation of matrix $\boldsymbol{A}$ but also avoids the variables of m, L', ν' and $\Delta t'$. Moreover, the larger N is, the larger ω is.

3. Code Validation and Grid Independence

In order to verify the reliability of the written computer code, the streamlines and isotherms of the natural convection in the concentric annulus were simulated using IB-LBM, and the comparison between the obtained results and literature [40] is shown in Figure 3. It is obvious that the obtained streamlines and isotherms are consistent with those in literature, so the validity of the present LBM code is guaranteed.

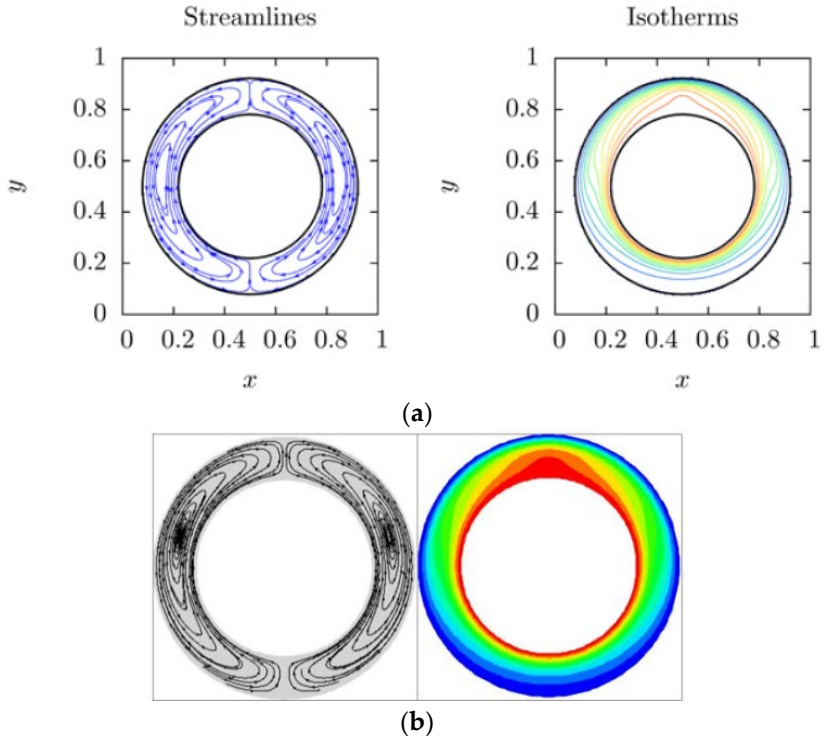

Figure 3. (**a**) The literature, (**b**) this work. Comparison of streamlines and isotherms obtained in this work and the literature.

To verify grid independency, different grid sizes of 120 × 120, 160 × 160, 200 × 200, 240 × 240 and 280 × 280 were tested in the case of $\lambda = 0.5$, $Ha = 40$ and $N = 0$, and the calculated average Nusselt numbers on the solid-fluid boundary are shown in Table 2. Clearly, the grid size of 200 × 200 would be the optimal choice to balance accuracy and computational time well.

Table 2. Effect of the grid size on the average Nusselt number.

Grid	120 × 120	160 × 160	200 × 200	240 × 240	280 × 280
Nu	3.96	4.11	4.17	4.18	4.18
Relative change	-	3.79%	1.46%	0.02%	0.00%

4. Results and Discussion

4.1. Effect of Rotational Speed on Streamlines and Isothermals

Figures 4 and 5 show the contours of stream function and dimensionless temperature at different N with $\lambda = 0.5$, $Ha = 0$ and $Ra = 10^6$, respectively. In Figure 4, the isolines of the stream function denote the streamlines; the absolute values of the numbers reflect the

relative magnitudes of the velocities; the sign of the numbers represents the flow direction: the positive value means the fluid is flowing anticlockwise along the isolines, while the negative value means that the fluid is flowing clockwise along the isolines; the gradient of the stream function can reflect the magnitude of velocity change.

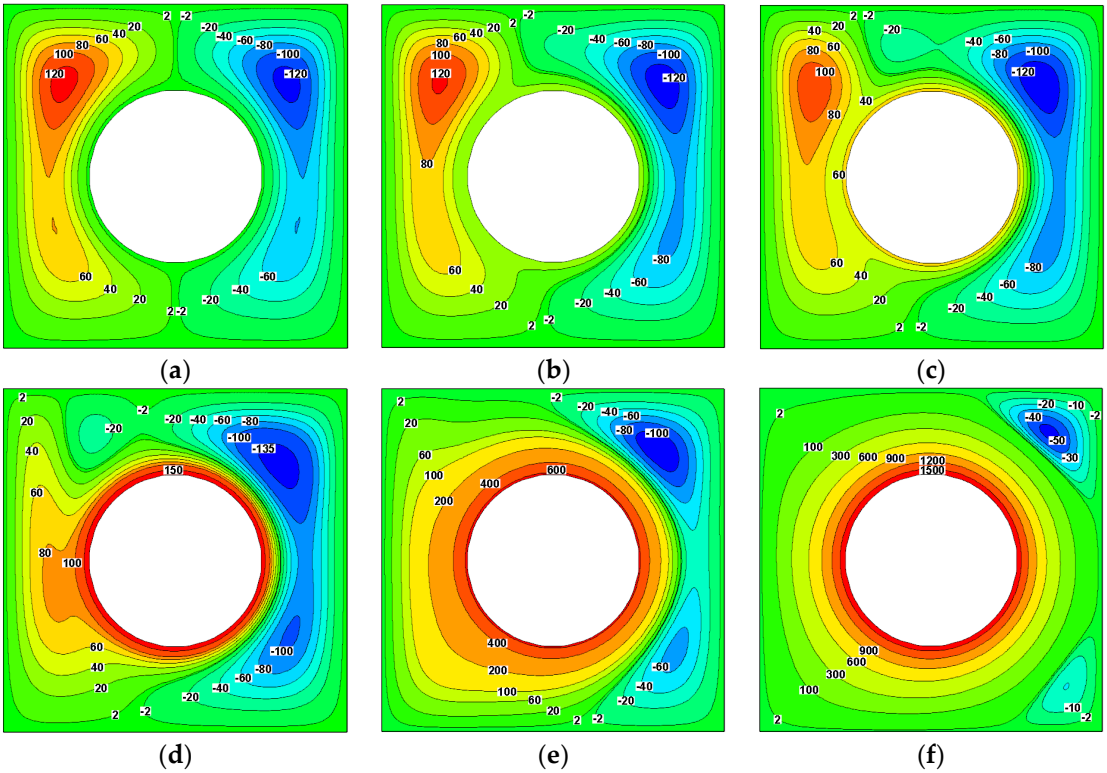

Figure 4. (**a**) $N = 0$, (**b**) $N = 10$, (**c**) $N = 20$, (**d**) $N = 50$, (**e**) $N = 100$, (**f**) $N = 200$. Contours of stream function at $\lambda = 0.5$, $Ha = 0$ and $Ra = 10^6$.

It can be learned from Figures 4 and 5 that the streamlines and isothermals are both generally symmetrical about the vertical center line at $N = 0$, and there exist two opposite vortexes flowing at relatively high velocity. Moreover, the average velocity and temperature at the top are much larger than those at the bottom, which is caused by the influence of gravity on flow and temperature distribution without rotation.

However, when N reaches 50, the anticlockwise vortex at the top left disappears but the clockwise vortex occurs at the bottom right; the maximum velocity is moving from the vortexes to the fluid around the rotating heat source due to the drive of rotation; the gradient of stream function on the right of the heat source is so large that the flow velocity changes rapidly there; though the average velocity and temperature at the top are still larger than those at the bottom, the gap between them narrows significantly, which indicates that the increase in rotational speed will reduce the effect of gravity on flow and temperature distribution.

Moreover, when N increases to 200, the vortexes at the top right and bottom right still exist, but the flow velocity is rather low compared to the zone adjacent to heat source; the gradient of flow velocity around the heat source becomes higher; it seems that the effect of gravity on the flow and temperature distribution has been removed in this case: the streamlines and isothermals are both generally symmetrical not only about the vertical center line but also about the horizontal center line. In other words, when the rotational speed increases up to a certain value, the effect of gravity on the flow and temperature distribution can be neglected because the rotation effect is the dominant factor influencing the velocity field and temperature field in this case.

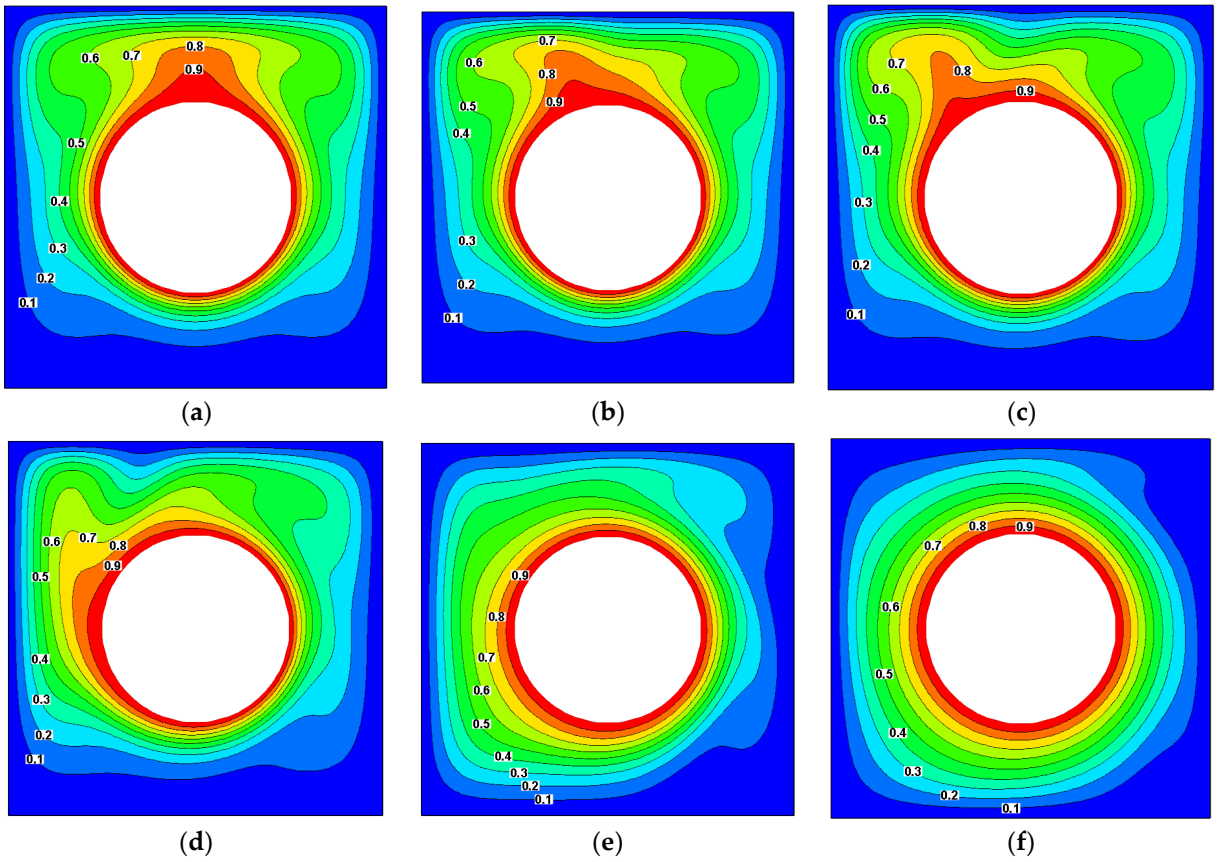

Figure 5. (**a**) $N = 0$, (**b**) $N = 10$, (**c**) $N = 20$, (**d**) $N = 50$, (**e**) $N = 100$, (**f**) $N = 200$. Contours of dimensionless temperature at $\lambda = 0.5$, $Ha = 0$ and $Ra = 10^6$.

4.2. Effect of Magnetic Field on Streamlines and Isothermals

Figures 6 and 7 show the contours of stream function and dimensionless temperature at different N with $\lambda = 0.5$, $Ha = 40$ and $Ra = 10^6$, respectively. Clearly, compared to Figures 4 and 5, the flow velocity in the same place (excluding the clockwise vortex at the bottom right) is decreasing more or less at the same N after the magnetic field is imposed on the nanofluid. In particular, at $N = 200$, a new clockwise vortex appears at the top left, and the area of anticlockwise flow driven by the rotating heat source becomes smaller.

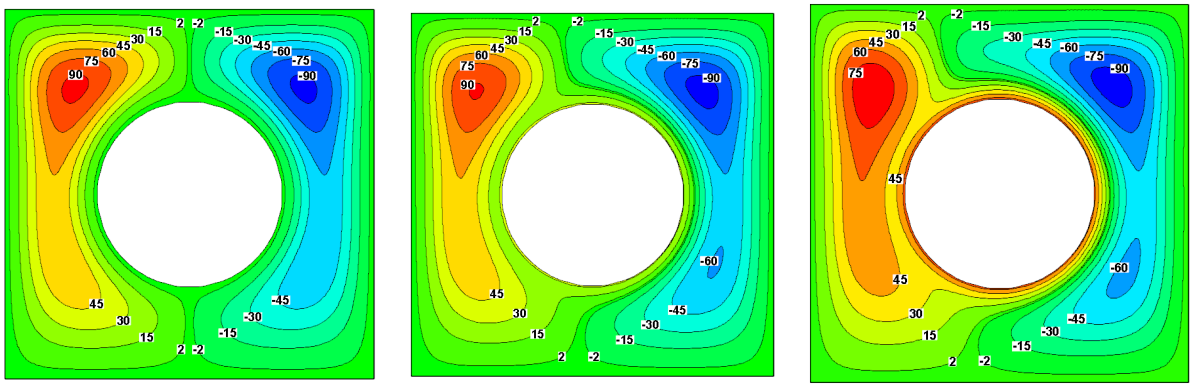

Figure 6. *Cont.*

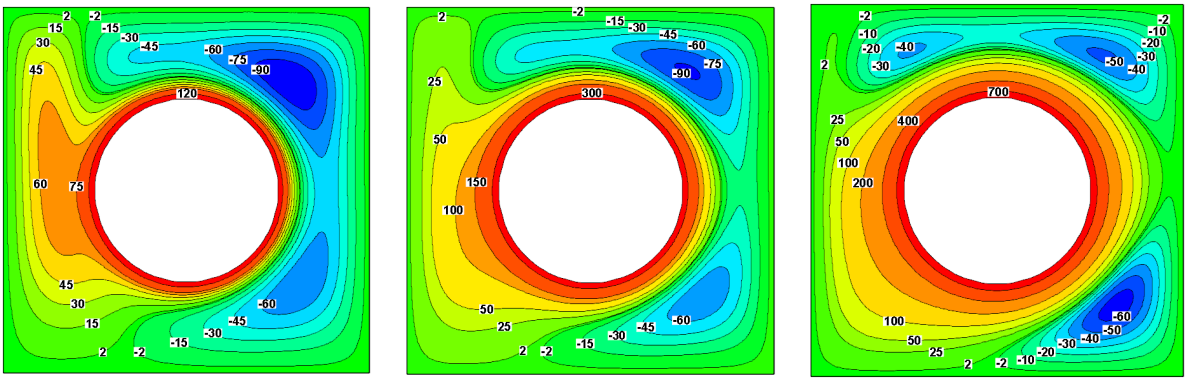

Figure 6. (**a**) $N = 0$, (**b**) $N = 10$, (**c**) $N = 20$, (**d**) $N = 50$, (**e**) $N = 100$, (**f**) $N = 200$. Contours of stream function at $\lambda = 0.5$, $Ha = 40$ and $Ra = 10^6$.

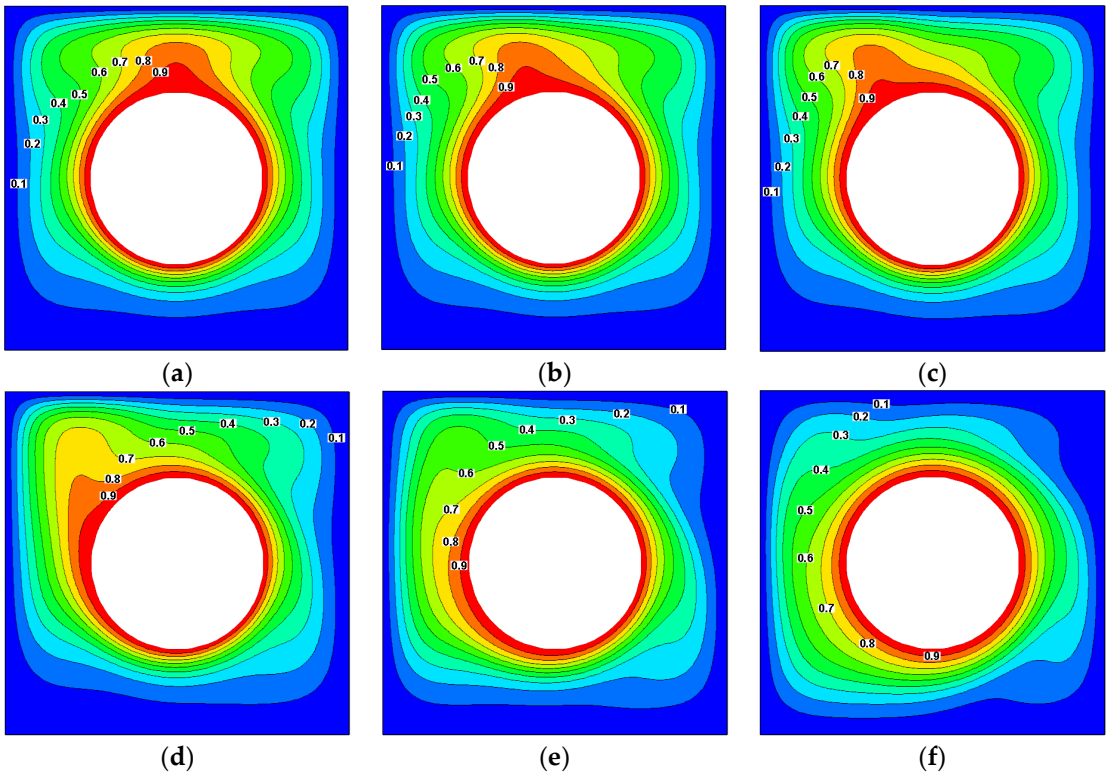

Figure 7. (**a**) $N = 0$, (**b**) $N = 10$, (**c**) $N = 20$, (**d**) $N = 50$, (**e**) $N = 100$, (**f**) $N = 200$. Contours of dimensionless temperature at $\lambda = 0.5$, $Ha = 40$ and $Ra = 10^6$.

What has been mentioned above may be due to the fact that the Lorenz force on the nanofluid generated by the magnetic field would suppress the flow and then have the retarding effect on the velocity field. In consequence, it is inferred that the imposed magnetic field will reduce the influence of rotation on the velocity field and temperature distribution.

4.3. Effect of Aspect Ratio on Streamlines and Isothermals

Figures 8 and 9 show the contours of stream function and dimensionless temperature at different N with $\lambda = 0.4$, $Ha = 40$ and $Ra = 10^6$, while Figures 10 and 11 show the contours of stream function and dimensionless temperature at different N with $\lambda = 0.3$, $Ha = 40$ and $Ra = 10^6$.

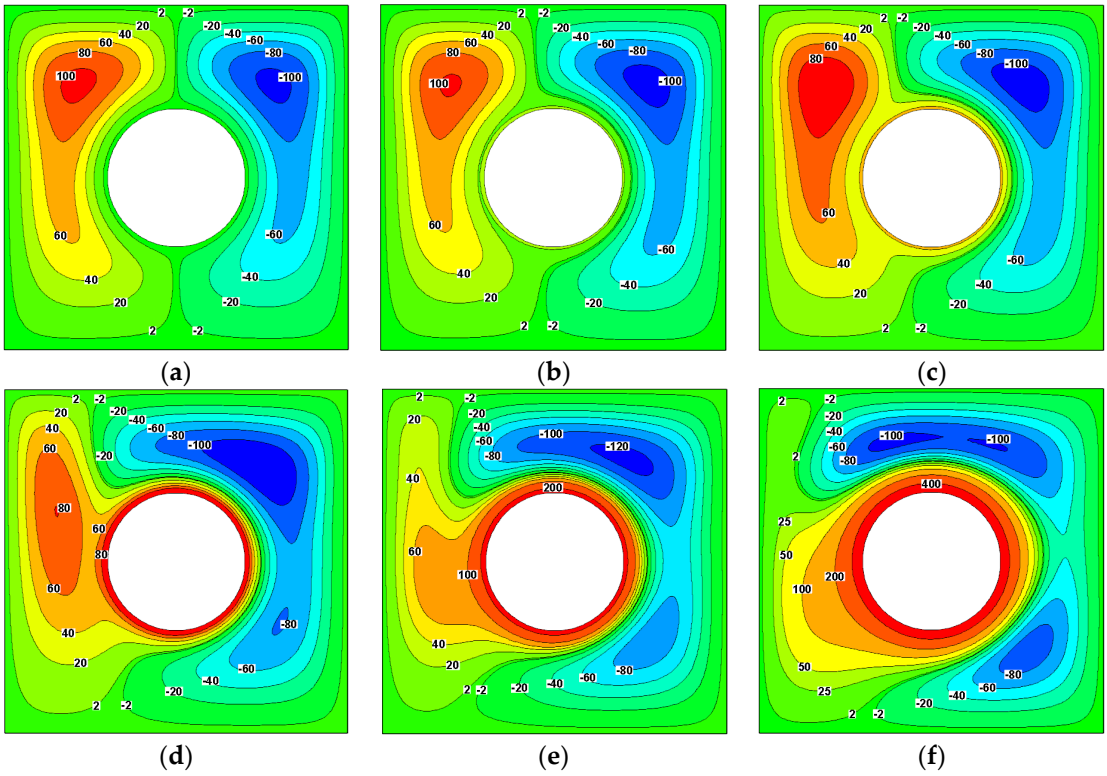

Figure 8. (**a**) $N = 0$, (**b**) $N = 10$, (**c**) $N = 20$, (**d**) $N = 50$, (**e**) $N = 100$, (**f**) $N = 200$. Contours of stream function at $\lambda = 0.4$, $Ha = 40$ and $Ra = 10^6$.

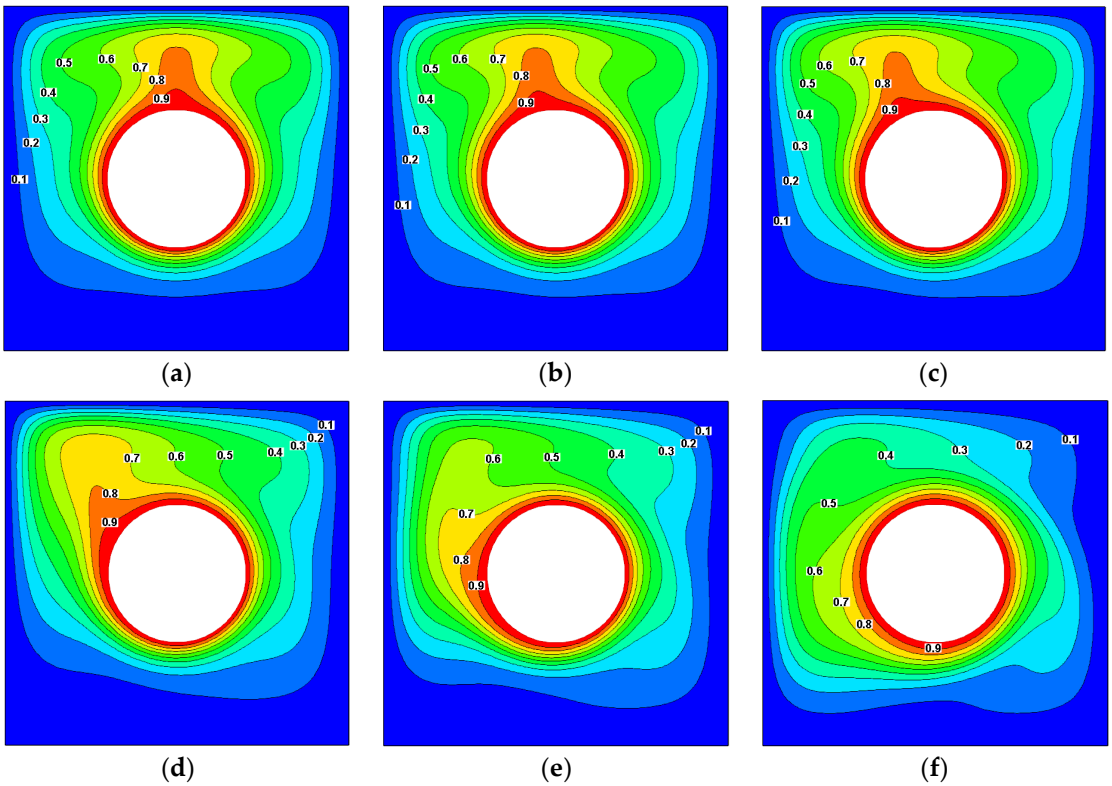

Figure 9. (**a**) $N = 0$, (**b**) $N = 10$, (**c**) $N = 20$, (**d**) $N = 50$, (**e**) $N = 100$, (**f**) $N = 200$. Contours of dimensionless temperature at $\lambda = 0.4$, $Ha = 40$ and $Ra = 10^6$.

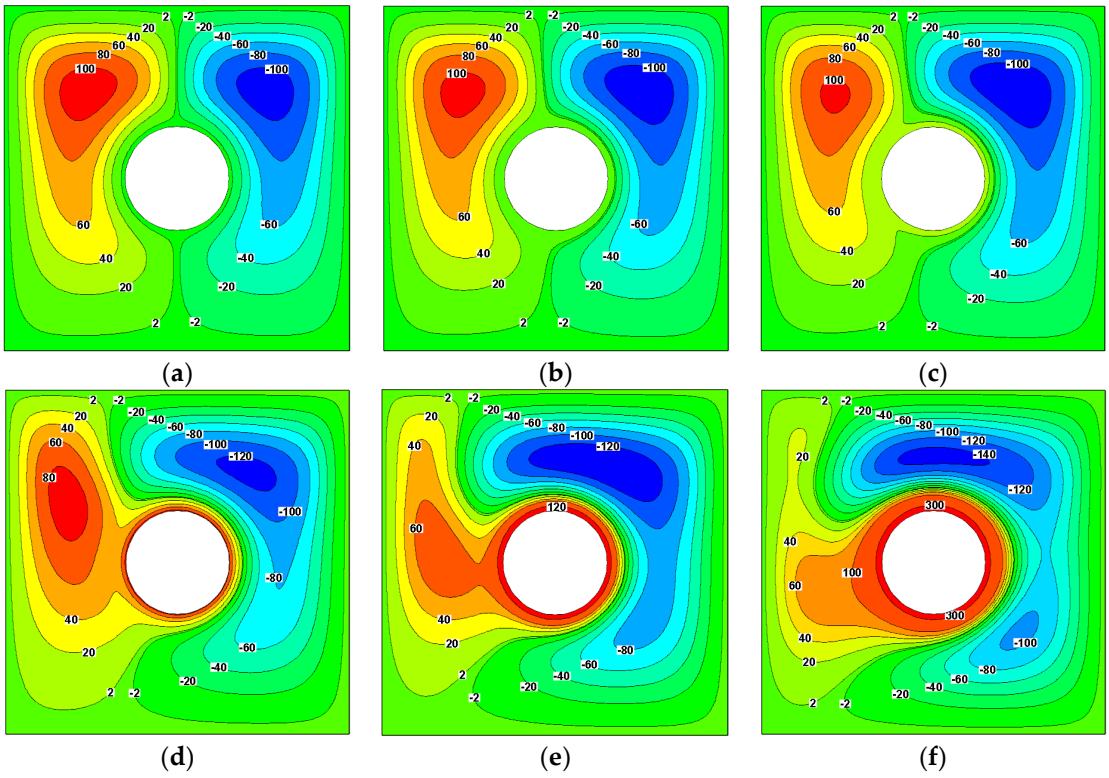

Figure 10. (**a**) $N = 0$, (**b**) $N = 10$, (**c**) $N = 20$, (**d**) $N = 50$, (**e**) $N = 100$, (**f**) $N = 200$. Contours of stream function at $\lambda = 0.3$, $Ha = 40$ and $Ra = 10^6$.

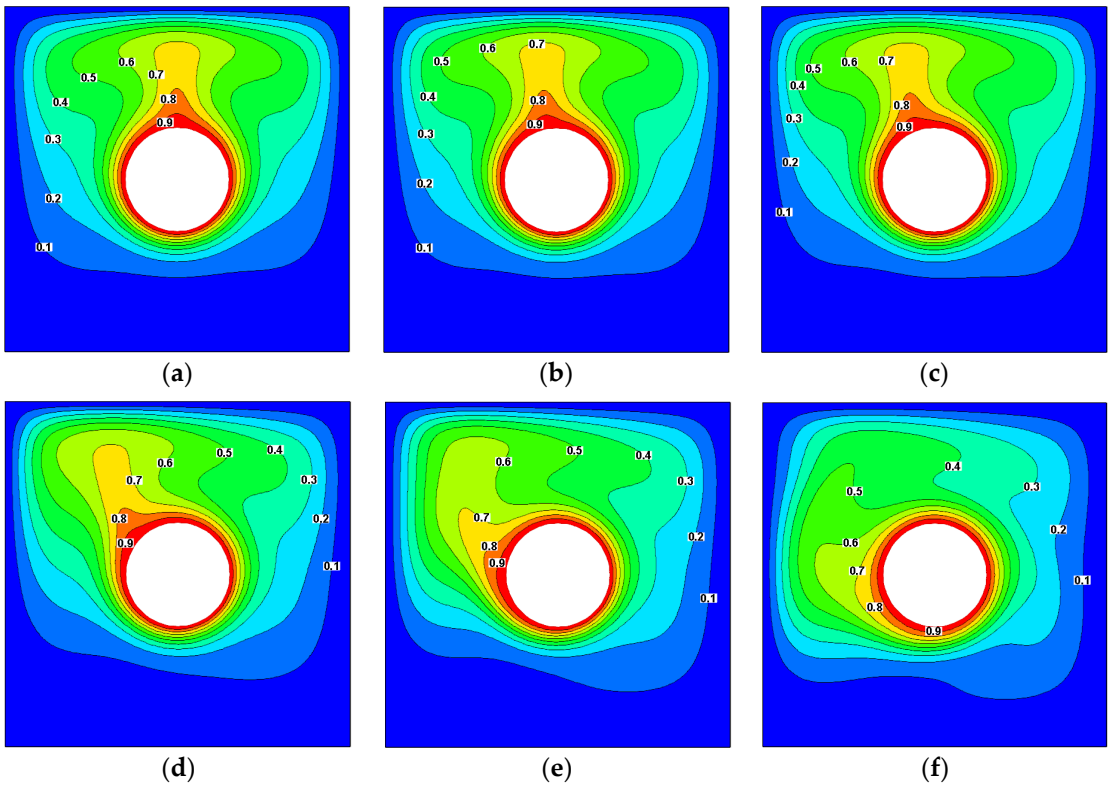

Figure 11. (**a**) $N = 0$, (**b**) $N = 10$, (**c**) $N = 20$, (**d**) $N = 50$, (**e**) $N = 100$, (**f**) $N = 200$. Contours of dimensionless temperature at $\lambda = 0.3$, $Ha = 40$ and $Ra = 10^6$.

It can be found out from Figures 8–11 that the velocity of the fluid around the rotating heat source decreases as λ decreases at the same N compared to Figure 6 because the decrease of λ at the same N will lead to a decrease in the linear velocity of the interface between fluid and heat source. On the contrary, the velocity of vortexes increases as λ decreases at the same N.

In addition, the isothermals become more and more asymmetric as λ decreases to 0.3 at N = 200, which is different from the case of λ = 0.5, where the isothermals still retain the characteristic of being roughly symmetrical about the horizontal center line after the magnetic field is imposed on the fluid. Thus, it is inferred that the retarding effect of the magnetic field on the rotation becomes more apparent at the smaller λ.

4.4. Effect of Rotational Speed on Average Nusselt Number

Figure 12 shows the trendlines of the average Nusselt number Nu on the surface of rotating heat source against N at different λ and Ha with $Ra = 10^6$. As seen, all the trendlines of Nu will fall off with the increase of N for all the presented cases, which may be owing to the reason that the velocity gradient of the fluid around the heat source will increase with the increase of N as well as the linear velocity of the solid-fluid boundary, leading to the decrease of Nu. For the same reason, Nu will decrease with the decrease of λ without considering other factors.

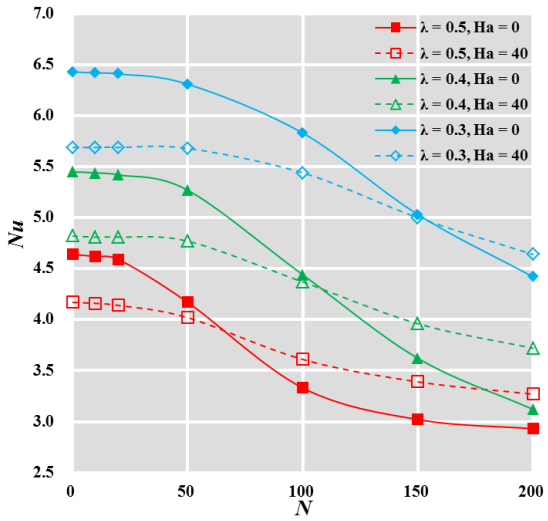

Figure 12. Effects of N on Nu in different cases.

Moreover, the additional magnetic field will reduce Nu at low N because the dominant natural convection will be suppressed by the Lorenz force in this case, while it will enhance Nu at high N because the rotation effect rather than the natural convection is dominant in this case and the velocity of the fluid around the heat source will be suppressed by the Lorenz force. Moreover, there exists a critical point N_c for each λ where the solid line and the dotted line in Figure 12 cross together, and the additional magnetic field has no influence on Nu at N_c. Clearly, N_c will increase with the decrease of λ.

5. Conclusions

In this study, the velocity field and temperature field inside the square cylinder with nanofluid and rotating heat source are numerically calculated, and the immersed boundary-lattice Boltzmann method is adopted to deal with the curved and moving solid-fluid boundary. Moreover, the dimensionless rotational speed N is proposed to save much computational time during the calculation. The following conclusions can be obtained by analyzing the results: Firstly, the increasing N will gradually suppress the effect of gravity on the flow and reduce the average Nusselt number Nu on the surface of the rotating heat source. Secondly, the external magnetic field will suppress the effect of rotation on the

flow, and it will reduce Nu at low N while increasing Nu at high N. Finally, the smaller λ will increase Nu and make the retarding effect of the magnetic field on the rotation more apparent. All the conclusions mentioned above will contribute to future work on expanding the applicability of the proposed techniques to three-dimensional simulations.

Author Contributions: Conceptualization, T.L. and X.L.; methodology, T.L. and J.X.; software, T.L.; validation, J.X., X.L. and M.H.; formal analysis, X.L.; investigation, J.X.; resources, M.H.; data curation, T.L. and J.X.; writing—original draft preparation, T.L.; writing—review and editing, T.L.; visualization, J.X.; supervision, X.L.; project administration, X.L.; funding acquisition, M.H. All authors have read and agreed to the published version of the manuscript.

Funding: This research was funded by [National Natural Science Foundation of China] grant number [51936009, 41941018, and 51721004] and [111 Project] grant number [B16038].

Acknowledgments: The support are provided by the National Natural Science Foundation of China (No. 51936009, 41941018, and 51721004), and the 111 Project (No. B16038) for the completion of this work are gratefully acknowledged.

Conflicts of Interest: I would like to declare on behalf of my co-authors that no conflict of interest exits in the submission of this manuscript, and manuscript is approved by all authors for publication. We confirm that the contents of this manuscript is an original research which have not been published previously, and not under consideration for publication elsewhere, in whole or in part.

References

1. Ashorynejad, H.R.; Zarghami, A. Magnetohydrodynamics flow and heat transfer of Cu-water nanofluid through a partially porous wavy channel. *Int. J. Heat Mass Transf.* **2018**, *119*, 247–258. [CrossRef]
2. Tayebi, T.; Chamkha, A.J. Entropy generation analysis due to MHD natural convection flow in a cavity occupied with hybrid nanofluid and equipped with a conducting hollow cylinder. *J. Therm. Anal. Calorim.* **2020**, *139*, 2165–2179. [CrossRef]
3. Alsabery, A.I.; Ismael, M.A.; Chamkha, A.J.; Hashim, I. Mixed convection of Al_2O_3-water nanofluid in a double lid-driven square cavity with a solid inner insert using Buongiorno's two-phase model. *Int. J. Heat Mass Transf.* **2018**, *119*, 939–961. [CrossRef]
4. Dogonchi, A.S.; Tayebi, T.; Chamkha, A.J.; Ganji, D.D. Natural convection analysis in a square enclosure with a wavy circular heater under magnetic field and nanoparticles. *J. Therm. Anal. Calorim.* **2020**, *139*, 661–671. [CrossRef]
5. Alsabery, A.I.; Ismael, M.A.; Chamkha, A.J.; Hashim, I.; Abulkhair, H. Unsteady flow and entropy analysis of nanofluids inside cubic porous container holding inserted body and wavy bottom wall. *Int. J. Mech. Sci.* **2021**, *193*, 106161. [CrossRef]
6. Radwan, A.; Ahmed, M. Thermal management of concentrator photovoltaic systems using microchannel heat sink with nanofluids. *Sol. Energy* **2018**, *171*, 229–246. [CrossRef]
7. Chamkha, A.; Ismael, M.; Kasaeipoor, A.; Armaghani, T. Entropy generation and natural convection of CuO-water nanofluid in C-shaped cavity under magnetic field. *Entropy* **2016**, *18*, 50. [CrossRef]
8. Tayebi, T.; Chamkha, A.J. Entropy generation analysis during MHD natural convection flow of hybrid nanofluid in a square cavity containing a corrugated conducting block. *Int. J. Numer. Methods Heat Fluid Flow* **2020**, *30*, 1115–1136. [CrossRef]
9. Selimefendigil, F.; Ismael, M.A.; Chamkha, A.J. Mixed convection in superposed nanofluid and porous layers in square enclosure with inner rotating cylinder. *Int. J. Mech. Sci.* **2017**, *124–125*, 95–108. [CrossRef]
10. Hu, Y.; Li, D.; Shu, S.; Niu, X. Natural convection in a nano fluid-filled eccentric annulus with constant heat flux wall: A lattice Boltzmann study with immersed boundary method. *Int. Commun. Heat Mass Transf.* **2017**, *86*, 262–273. [CrossRef]
11. Mahmoudi, A.; Mejri, I.; Abbassi, M.A.; Omri, A. Lattice Boltzmann simulation of MHD natural convection in a nanofluid-filled cavity with linear temperature distribution. *Powder Technol.* **2014**, *256*, 257–271. [CrossRef]
12. Sathiyamoorthy, M.; Chamkha, A. Effect of magnetic field on natural convection flow in a liquid gallium filled square cavity for linearly heated side wall(s). *Int. J. Therm. Sci.* **2010**, *49*, 1856–1865. [CrossRef]
13. Izadi, S.; Armaghani, T.; Ghasemiasl, R.; Chamkha, A.J.; Molana, M. A comprehensive review on mixed convection of nanofluids in various shapes of enclosures. *Powder Technol.* **2019**, *343*, 880–907. [CrossRef]
14. Alsabery, A.I.; Gedik, E.; Chamkha, A.J.; Hashim, I. Impacts of heated rotating inner cylinder and two-phase nanofluid model on entropy generation and mixed convection in a square cavity. *Heat Mass Transf. Und Stoffuebertragung* **2020**, *56*, 321–338. [CrossRef]
15. Upadhya, S.M.; Devi, R.L.V.R.; Raju, C.S.K.; Ali, H.M. Magnetohydrodynamic nonlinear thermal convection nanofluid flow over a radiated porous rotating disk with internal heating. *J. Therm. Anal. Calorim.* **2020**, *143*, 1973–1984. [CrossRef]
16. Jeyabalan, S.R.; Chertovskih, R.; Gama, S.; Zheligovsky, V. Nonlinear Large-Scale Perturbations of Steady Thermal Convective Dynamo Regimes in a Plane Layer of Electrically Conducting Fluid Rotating about the Vertical Axis. *Mathematics* **2022**, *10*, 2957. [CrossRef]
17. Chertovskih, R.; Gama, S.M.A.; Podvigina, O.; Zheligovsky, V. Dependence of magnetic field generation by thermal convection on the rotation rate: A case study. *Phys. D Nonlinear Phenom.* **2010**, *239*, 1188–1209. [CrossRef]

18. Rashidi, M.M.; Abelman, S.; Mehr, N.F. Entropy generation in steady MHD flow due to a rotating porous disk in a nanofluid. *Int. J. Heat Mass Transf.* **2013**, *62*, 515–525. [CrossRef]
19. Sheikholeslami, M.; Gorji-Bandpy, M.; Ganji, D.D. Lattice Boltzmann method for MHD natural convection heat transfer using nanofluid. *Powder Technol.* **2014**, *254*, 82–93. [CrossRef]
20. Feng, Z.G.; Michaelides, E.E. The immersed boundary-lattice Boltzmann method for solving fluid-particles interaction problems. *J. Comput. Phys.* **2004**, *195*, 602–628. [CrossRef]
21. Wu, J.; Shu, C. Implicit velocity correction-based immersed boundary-lattice Boltzmann method and its applications. *J. Comput. Phys.* **2009**, *228*, 1963–1979. [CrossRef]
22. Hu, Y.; Li, D.; Shu, S.; Niu, X. Immersed boundary-lattice Boltzmann simulation of natural convection in a square enclosure with a cylinder covered by porous layer. *Int. J. Heat Mass Transf.* **2016**, *92*, 1166–1170. [CrossRef]
23. Li, D.; Zhang, H.; Ye, P.; Yu, Z. Natural convection of power-law nanofluid in a square enclosure with a circular cylinder: An immersed boundary-lattice boltzmann study. *Int. J. Mod. Phys. C* **2018**, *29*, 1850105. [CrossRef]
24. Kang, S.K.; Hassan, Y.A. A comparative study of direct-forcing immersed boundary-lattice Boltzmann methods for stationary complex boundaries. *Int. J. Numer. Methods Fluids* **2011**, *66*, 1132–1158. [CrossRef]
25. Chamkha, A.J. MHD-free convection from a vertical plate embedded in a thermally stratified porous medium with Hall effects. *Appl. Math. Model.* **1997**, *21*, 603–609. [CrossRef]
26. Veera Krishna, M.; Ameer Ahamad, N.; Chamkha, A.J. Hall and ion slip impacts on unsteady MHD convective rotating flow of heat generating/absorbing second grade fluid. *Alex. Eng. J.* **2021**, *60*, 845–858. [CrossRef]
27. Veerakrishna, M.; Subba Reddy, G.; Chamkha, A.J. Hall effects on unsteady MHD oscillatory free convective flow of second grade fluid through porous medium between two vertical plates. *Phys. Fluids* **2018**, *30*, 23106. [CrossRef]
28. Krasnov, D.S.; Zienicke, E.; Zikanov, O.; Boeck, T.; Thess, A. Numerical study of the instability of the Hartmann layer. *J. Fluid Mech.* **2004**, *504*, 183–211. [CrossRef]
29. Rahmati, A.R.; Tahery, A.A. Numerical study of nanofluid natural convection in a square cavity with a hot obstacle using lattice Boltzmann method. *Alex. Eng. J.* **2018**, *57*, 1271–1286. [CrossRef]
30. Vijaybabu, T.R.; Dhinakaran, S. MHD Natural convection around a permeable triangular cylinder inside a square enclosure filled with $Al_2O_3-H_2O$ nanofluid: An LBM study. *Int. J. Mech. Sci.* **2019**, *153–154*, 500–516. [CrossRef]
31. Lai, T.; Liu, X.; Xue, S.; Xu, J.; He, M.; Zhang, Y. Extension of Ergun equation for the calculation of the flow resistance in porous media with higher porosity and open-celled structure. *Appl. Therm. Eng.* **2020**, *173*, 115262. [CrossRef]
32. Guo, Z.; Shu, C. *Lattice Boltzmann Method and Its Applications in Engineering*; World Scientific: Singapore, 2013.
33. Zarghami, A.; Di Francesco, S.; Biscarini, C. Porous substrate effects on thermal flows through a rev-scale finite volume lattice boltzmann model. *Int. J. Mod. Phys. C* **2014**, *25*, 1350086. [CrossRef]
34. Sheikholeslami, M.; Gorji-Bandpy, M.; Vajravelu, K. Lattice Boltzmann simulation of magnetohydrodynamic natural convection heat transfer of Al_2O_3-water nanofluid in a horizontal cylindrical enclosure with an inner triangular cylinder. *Int. J. Heat Mass Transf.* **2015**, *80*, 16–25. [CrossRef]
35. Wu, J.; Shu, C.; Zhao, N. Simulation of thermal flow problems via a hybrid immersed boundary-lattice Boltzmann method. *J. Appl. Math.* **2012**, *2012*, 161484. [CrossRef]
36. Dong, B.; Zhou, X.; Zhang, Y.; Chen, C.; Li, W. Numerical simulation of thermal flow of power-law fluids using lattice Boltzmann method on non-orthogonal grids. *Int. J. Heat Mass Transf.* **2018**, *126*, 293–305. [CrossRef]
37. Fu, J.; Zhang, T.; Li, M.; Li, S.; Zhong, X.; Liu, X. Study on flow and heat transfer characteristics of porous media in engine particulate filters based on lattice Boltzmann method. *Energies* **2019**, *12*, 3319. [CrossRef]
38. Kang, X.; Liao, Q.; Zhu, X.; Yang, Y. Non-equilibrium extrapolation method in the lattice Boltzmann simulations of flows with curved boundaries (non-equilibrium extrapolation of LBM). *Appl. Therm. Eng.* **2010**, *30*, 1790–1796. [CrossRef]
39. Yang, Y.; Liao, Q.; Zhu, X.; Wang, H.; Wu, R.; Lee, D.J. Lattice Boltzmann simulation of substrate flow past a cylinder with PSB biofilm for bio-hydrogen production. *Int. J. Hydrogen Energy* **2011**, *36*, 14031–14040. [CrossRef]
40. Wei, Y.; Wang, Z.; Qian, Y.; Guo, W. Study on bifurcation and dual solutions in natural convection in a horizontal annulus with rotating inner cylinder using thermal immersed boundary-lattice Boltzmann method. *Entropy* **2018**, *20*, 733. [CrossRef]